Microscopic liquid-gas interface effect on liquid wetting

Zhang, J.; Ding, W.; Wang, Z.; Wang, H.; Hampel, U.;

Originally published:

October 2022

Journal of Colloid and Interface Science 630(2023), 813-822

DOI: https://doi.org/10.1016/j.jcis.2022.10.062

Perma-Link to Publication Repository of HZDR:

https://www.hzdr.de/publications/Publ-35321

Microscopic liquid-gas interface effect on liquid wetting

Jinming Zhang[a], *Wei Ding*[a,*], *Zuankai Wang*[c], *Hao Wang*[d], *Uwe Hampel*[a,b]

[a]Helmholtz-Zentrum Dresden-Rossendorf (HZDR), Institute of Fluid Dynamics, Dresden 01328, Germany

[b]Technische Universität Dresden, Institute of Power Engineering, Dresden 01062, Germany

[c]Department of Mechanical Engineering, City University of Hong Kong, Hong Kong SAR 999077, China

[d]The Laboratory of Heat and Mass Transport at Micro-Nano Scale, College of Engineering, Peking University, Beijing 100871, China

Jinming Zhang email address: j.zhang@hzdr.de

Wei Ding email address: w.ding@hzdr.de

Zuankai Wang email address: zuanwang@cityu.edu.hk

Hao Wang email address: hwang@coe.pku.edu.cn

Uwe Hampel email address: u.hampel@hzdr.de

Corresponding Author

Wei Ding - Helmholtz-Zentrum Dresden-Rossendorf (HZDR), Institute of Fluid Dynamics, Dresden 01328, Germany; Email: w.ding@hzdr.de

Phone: +49-351-260 2170

FAX: +49 351 260 2383

Abstract:

Hypothesis: Young contact angle is widely applied to evaluate liquid wetting phenomena on solid surfaces. For example, it gives a truncated-spherical shape prediction of a droplet profile through the Young-Laplace equation. However, recent measurements have shown deviations between microscopic droplet profiles and the spherical shape, indicating that the conventional Young contact angle is insufficient to describe microscopic wetting phenomena. In this work, we hypothesize that a liquid-gas interface nano-bending, which is caused by the nonlinear coupling between the effects of the microscopic interface geometry and solid-liquid interactions, is responsible for this deviation.

Simulation and theory: Using molecular dynamics simulations and mathematical modeling, we reveal the structure of the nano-bending and the mechanism of the nonlinear-coupled effect. We further apply our findings to illustrate a liquid microlayer with the saddle-shaped profile in nucleate boiling.

Findings: The nonlinear-coupled effect is responsible for the deviation of a nano-droplet profile and also the very thin microlayer captured by different experiments. The saddle-shaped interface significantly highlights the nonlinear-coupled effect. The interface nano-bending, rather than the Young contact angle, acts as the boundary condition and dictates the liquid wetting system, especially for the case with high interface curvature. These findings provide insight into recent nano-scale droplet- and bubble-related wetting phenomena.

KEYWORDS: liquid wetting, nano-bending, nonlinear-coupled effect, interface curvature, Young contact angle, nano-droplet, nano-bubble, microlayer, nucleate boiling

1. Introduction

Liquid wetting on surfaces is ubiquitous in nature and is of great scientific and technological interest [1–4]. Recent examples such as liquid directional steering [5], surface curvature-driven droplet motion [6], ultra-thin water film evaporation [7,8], and triboelectric nanogenerators [9,10] have illustrated the beauty of the wetting phenomena by tailoring the solid surface properties,

including curvature, roughness, and chemistry. Despite its seeming simplicity, understanding these intriguing liquid-wetting behaviors requires probing the complex solid-liquid interaction that manifests itself as the contact angle [11].

Conventionally, the Young contact angle is central to describing a wetting system since it provides the critical boundary condition for the bulk liquid [12,13]. For example, the equilibrium droplet profile on an ideal surface is dictated by the Young contact angle through the Young-Laplace equation

$$P_g - P_l = P_c, \tag{1}$$

in which P_g and P_l are the pressure in the gas and liquid phase. P_c is the capillary pressure induced by the interface curvature $P_c = \sigma K$. σ is the liquid-gas interface surface tension, and K is the interface curvature. The prediction of Eq. 1 provides a truncated-spherical shape of the droplet profile. On the contrary, experimentally observed nano-scale droplet profiles have always exhibited a meniscus within 20 nm thickness from the contact line even on smooth and homogeneous surfaces [14–16]. This deviates from the prediction based on the Young contact angle. In a recent experimental measurement of the nano-droplet profile, Samoila *et al.* obtained completely different contact angles of the nano-droplets with different volumes on the same surface [17]. This indicates that the Young contact angle as the boundary condition is insufficient to describe the nano-scale wetting phenomena. Therefore, an exact mechanism to explain the deviation can be crucial to numerous nano-scale wetting-related phenomena, *e.g.,* interfacial mass transport [18,19] and contact line dynamics [20,21].

To account for this deviation, the effect of the solid-liquid molecular interaction [17,19,22] near the contact line has been investigated extensively. The solid-liquid interaction gives rise to the scale-dependent surface molecular forces and distorts the gas-liquid interface. In addition, the contact angle of a droplet below a critical size has been found dependent on the droplet size [16,23,24], *i.e.,* the line tension effect. Although descriptions of both effects have been well established in the past decades, there seems to exist an internal connection that is still confusing. Indeed, surface molecular forces can strongly influence the interface curvature [25]. On the other hand, the line tension, as a manifestation of surface molecular forces near the contact line, is dependent on the curvature of the gas-liquid interface [26,27]. Interestingly, a recent molecular

dynamics (MD) simulation suggested that the effect of gas-liquid interface curvature and the effect of surface molecular forces are entangled [28]. This is not surprising given that these two effects have an identical origin, *i.e.,* molecular interactions [29]. However, the entanglement brings difficulties in understanding how a nano-scale droplet profile deviates. An insight into the entangled relationship between the effect of surface molecular forces and the effect of the gas-liquid interface curvature is needed.

The interface curvature of a 3D axisymmetric droplet is characterized by two principal curvatures κ_1, κ_2 as $K = \kappa_1 + \kappa_2 = \frac{\delta''}{(1+\delta'^2)^{\frac{3}{2}}} + \frac{\delta'}{r(1+\delta'^2)^{\frac{1}{2}}}$ (**Fig. 1a)**. δ represents the height of the droplet profile, and r is the radius. However, the principal curvatures of a droplet have the same signs: $\kappa_1\kappa_2 > 0$, that is, the capillary pressure caused by both principal curvatures increases the liquid pressure and promotes the formation of a spherical droplet. In this case, the deviation of an actual droplet profile only occurs at the microscopic scale, thus veiling the physics of the entangled effect.

An interesting case of a surface wetting configuration with principal curvatures of different signs is the microlayer in the inertia-controlled bubble growth stage in nucleate boiling, which is a μ-meter thin liquid film trapped underneath a rapidly growing bubble. Besides being of practical importance for heat transfer applications [30–32], the microlayer is a good example to illustrate the entangled effect of the contact line geometry and surface molecular forces. Unlike the spherical droplet (**Fig. 1a**), the 3D profile of the microlayer is saddle-shaped (**Fig. 1b**) and $\kappa_1\kappa_2 < 0$. In this case, the capillary pressure induced by interface curvatures can be understood to both increase and decrease the liquid pressure, depending on the direction of the principal curvature.

The accurate description of the microlayer has been a challenge for decades. Previous works mainly resort to DNS simulations and mechanistic models to tackle the hydrodynamic part of this problem [31,33–35], which failed to explain the very thin microlayer obtained in recent experiments [36–38]. It is also worthy mentioning that some recent microlayer simulations have achieved comparable thickness with the experiment results by considering the effects of microlayer evaporation [39–41] and contact line dewetting [42,43]. Nevertheless, the obvious microlayer evaporation and the contact line dewetting were observed only after the early stage [36,44,45], referred to as the diffusion-controlled bubble growth stage [46].

This work aims to reveal how the effect of surface molecular forces and the effect of the gas-liquid interface curvature are entangled. We first studied the entangled effects on the deviation of a 3D nano-droplet profile by using MD simulations. Then we developed a three-region description of the microlayer (**Fig. 1b**) that considers the entangled effects of surface molecular forces and gas-liquid interface curvature. We elucidated the relationship between the effect of surface molecular forces and the effect of the gas-liquid interface curvature. We found that the mechanism responsible for the deviation of a nano-droplet profile can explain the very thin microlayer, though the detailed manifestations of the entanglement are different in the context of the nano-droplet and microlayer.

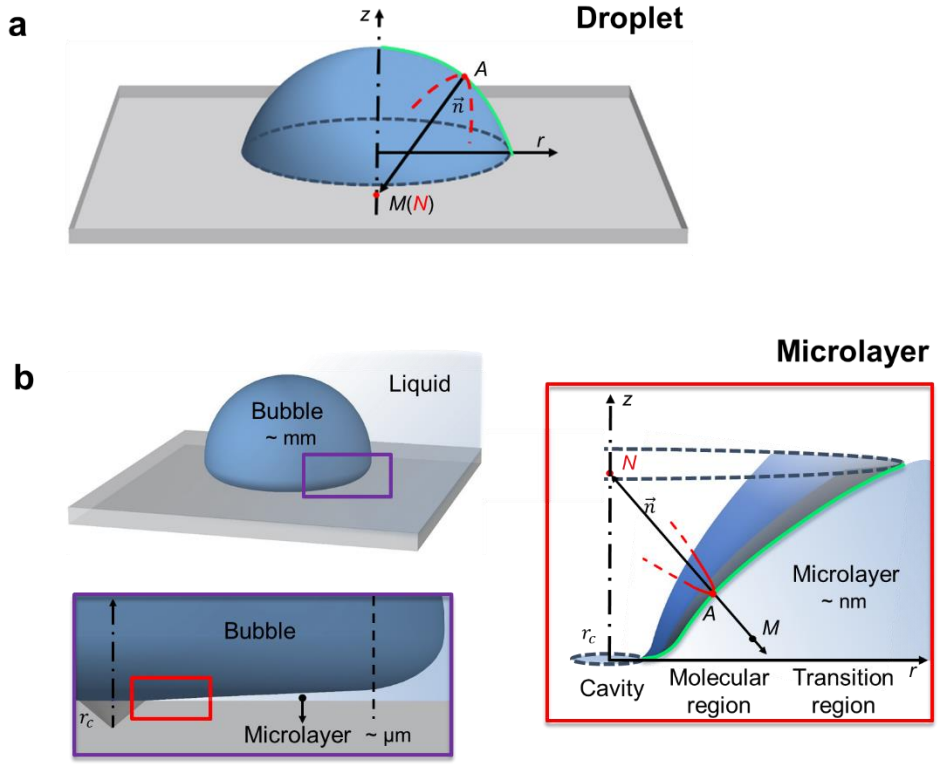

Fig. 1. Geometry configurations of surface wetting examples. (**a**) Schematic of a 3D droplet on a solid surface. $\overrightarrow{AM}$ and $\overrightarrow{AN}$ are the radii of the principal curvatures κ_1 and κ_2 of the gas-liquid interface (Green line). (**b**) Schematic of a 3D multiscale microlayer underneath a growing bubble in the inertia-controlled bubble growth stage in nucleate boiling. The microlayer consists of a molecular region, a transition region, and a hydrodynamic region. The molecular region starts from the edge of a cavity, followed by the transition region and the hydrodynamic region of the

microlayer. r_c is the radius of the cavity. $\overrightarrow{\mathrm{AM}}$ and $\overrightarrow{\mathrm{AN}}$ are the radii of the principal curvatures κ_1 and κ_2 of the microlayer vapor-liquid interface (Green line).

2. Methods

2.1 Molecular dynamics simulation

The equilibrium 3D nano-droplets on silicon (1 0 0) substrate are simulated to investigate the entangled effect of surface molecular forces and the interface curvature by using MD simulations via the LAMMPS software package [47]. Specifically, we vary the footprint radii of the droplet (5 nm, 7.5 nm, and 10 nm) to account for the effect of the interface curvature. The surface molecular forces between water molecules and silicon atoms are modeled by the 12-6 L-J potential via silicon and oxygen atoms with the parameters $\sigma_{\mathrm{Si-O}} = 3.41$ Å and $\varepsilon_{\mathrm{Si-O}} = 1.457$ KJ/mol [48]. The water is modeled by the SPC/E model. The interaction between oxygen and hydrogen atoms is modeled by the long-range Coulombic potential. The cutoff distance for LJ potential is set as 15 Å. The water molecules are initialized at 1 K in a rectangular box away from the surface and then the temperature is increased to 300 K with an increment of 50 K. Each temperature increment phase is 50 ps. The temperature is maintained at 300 K for another 250 ps to reach equilibrium. The droplet is then brought to the substrate within 3 Angstrom. The spreading and equilibration of the droplet on the surface are for 3 ns. The entire simulation is carried out in the canonical (NVT) ensembles at 300 K using a Nosé-Hoover thermostat. To obtain the statistical droplet profile, we record the positions of water molecules with 1 ps interval in the final 0.2 ns.

2.2 Liquid-gas interface shape model

We employ the augmented Young-Laplace equation to account for the entangled effect of surface molecular forces and gas-liquid interface curvature, given as

$$P_g - P_l = P_c + P_d, \tag{2}$$

where P_d is the disjoining pressure, originating from the surface molecular forces acting on the liquid phase in the equilibrium state [49]. The augmented Young-Laplace equation coupled with various disjoining pressure has been applied in numerous microscopic liquid droplet/film problems [17,50,51]. However, the entangled effect has never been recognized. The main reason is that liquid with infinite size was considered in most cases. In Eq. 2, we consider the entangled effect

as a sum of the capillary pressure and the disjoining pressure to determine the liquid-gas interface shape. According to the extended DLVO theory, the disjoining pressure, P_d, mainly includes four components $P_d = P_{vdW} + P_{st} + P_{ha} + P_{dl}$ [25,52,53], where P_{vdW} is the van der Waals force, P_{st} is steric repulsion, P_{ha} is hydrophobic attraction force, P_{ha} is the electrostatic double-layer force. These four components can cover non-covalent interactions, such as for a silicon-water-vapor system [53].

Van der Waals force is expressed as $P_{vdW} = -\frac{A}{\delta^3}$ [25,53]. A is the Hamaker constant, which is related to the solid-liquid van der Waals interaction energy by $A = 12\pi\Delta G^{LW} d_0$. ΔG^{LW} is the solid-liquid Lifshitz–van der Waals interaction free energy, d_0 is the minimum equilibrium distance between two condensed-phase surfaces and is considered a constant of 0.157 nm [53]. The steric repulsion arises at very small distances to the adsorbed film on a surface. A commonly-used expression of steric repulsion is given by $P_{st} = -\frac{B}{\delta^9}$. B equals to $6A\delta_0^6$ [25]. δ_0 is the thickness of the adsorbed thin film on a given surface. The hydrophobic attraction force can originate when the water molecules near surfaces are induced to order into layers with orientation structure. There is still no universal law for hydrophobic attraction. Here we adopt the expression as $P_{ha} = \Delta G^{AB} e^{-\delta/\lambda} + \Delta G_d^{AB} e^{-\delta/\lambda_d}$ [52,54]. The first term is the short-range hydrophobic force, ΔG^{AB} is the liquid-solid polar interactive free energy. λ is the water characteristic decay length and has to be obtained from experiments. The second term represents the long-range hydrophobic force, whereby ΔG_d^{AB} is considered 1000 times less than ΔG^{AB} according to the previous force measurements [55]. λ_d is by one order of magnitude larger than λ [54]. Electrostatic double-layer force can play a strong role in long-range interactions between electrolytes and a solid surface [56]. However, it exists only between charged molecules (ions) or surfaces and depend on the electrolyte concentration [57]. We examined the contribution of the electrostatic double-layer force to the overall surface molecular forces and found that the electrostatic double-layer force is much weaker compared to other components for the deionized water (A detailed description can be found in the **Supporting Information)**. Therefore, we only consider three types of the surface molecular forces, i.e., $P_d = P_{vdW} + P_{st} + P_{ha}$. Note that the disjoining pressure reduces the liquid pressure when it is repulsive.

The considered surface molecular forces are defined in terms of solid-liquid-gas interaction free energy ΔG_{slv}. Based on the Dupré equation $\Delta G_{slv} = \gamma_{sl} - \gamma_{sg} - \gamma_{lg}$, we can express the disjoining pressure P_d by interfacial energy γ_{sl}, γ_{sg}, and γ_{lg}. Then, the interfacial energy γ_{sl} can be further related to the surface energy γ_s and γ_l based on the multi-component approach by Oss $\gamma_{sl} = (\sqrt{\gamma_s^{LW}} - \sqrt{\gamma_l^{LW}})^2 + 2(\sqrt{\gamma_s^+} - \sqrt{\gamma_l^+})(\sqrt{\gamma_s^-} - \sqrt{\gamma_l^-})$ [58], where γ_s^{LW}, γ_s^+ and γ_s^- are the Lifshitz–van der Waals surface energy and the polar Lewis acid-base surface energy. Note γ_g is zero in this work. Therefore, the disjoining pressure for a fixed wetting liquid is determined by the surface energy, which can be obtained by measuring the contact angle of three different liquids on the surface. The expression of the disjoining pressure and the derived relationship between interaction free energy and surface energy are summarized in **Table 1**. For the sake of simplicity, we shall name the above-mentioned augmented Young-Laplace equation coupled with the multi-component approach as the **M model.** The calculation methods for the M model can be found in the **Supporting Materials**.

The M model provides us with a general mathematical formula to describe the liquid-gas interface profile on any given surface. To validate the M model, we compare the predicted profile by the M model with the MD simulated profile. As shown in **Fig. 2**, a good agreement indicates the validity of the M model for the considered case. Note that the M model cannot capture the details of the droplet profile on the sub-nanoscale. It is because the actual footprint radii of the nano-droplet in MD simulation are difficult to determine when we consider Diaz's approach, which considers a zero slope of the profile at the contact line [59].

Table 1. Components of the M model: disjoining pressure and its relationship with surface energy

Van der Waals force P_{vdW}	$P_{vdW} = -\frac{A}{\delta^3}$ [25]; A: Hamaker constant, $A = 12\pi\Delta G^{LW} d_0$; ΔG^{LW}: liquid-solid Lifshitz-van der Waals interaction free energy;

	d_0 : minimum equilibrium distance between two condensed phase surfaces = 0.157 nm [53]
Steric repulsion P_{st}	$P_{st} = -\frac{B}{\delta^9}$ [25]; B = $6A\delta_0^6$; δ_0 : thickness of the adsorbed thin film on a given surface
Hydrophobic attraction force P_{ha}	$P_{ha} = \Delta G^{AB} e^{-\delta/\lambda} + \Delta G_d^{AB} e^{-\delta/\lambda_d}$ [52,54] ΔG^{AB} : liquid-solid polar interaction free energy; λ: water characteristic decay length; $\Delta G_d^{AB} = \Delta G^{AB}/1000$ [55], $\lambda_d > 10\ \lambda$[54] $\Delta G^{AB} e^{-\delta/\lambda}$: short-range hydrophobic force $\Delta G_d^{AB} e^{-\delta/\lambda_d}$: long-range hydrophobic force
Lifshitz-van der Waals interaction free energy ΔG^{LW}	$\Delta G^{LW} = 2[\sqrt{\gamma_s^{LW}\gamma_l^{LW}} + \sqrt{\gamma_g^{LW}\gamma_l^{LW}} - \sqrt{\gamma_s^{LW}\gamma_g^{LW}} - \gamma_l^{LW}]$ [58], γ^{LW}: Lifshitz–van der Waals surface energy
Polar interaction free energy ΔG^{AB}	$\Delta G^{AB} = 2[\sqrt{\gamma_l^+}\left(\sqrt{\gamma_s^-} + \sqrt{\gamma_g^+} - \sqrt{\gamma_l^-}\right) - \sqrt{\gamma_l^-}\left(\sqrt{\gamma_s^+} + \sqrt{\gamma_g^+} - \sqrt{\gamma_v^+}\right) - \sqrt{\gamma_s^+\gamma_g^-} - \sqrt{\gamma_s^-\gamma_g^+}]$ [58], γ^+ and γ^- : the polar Lewis acid-base surface energy

199

200

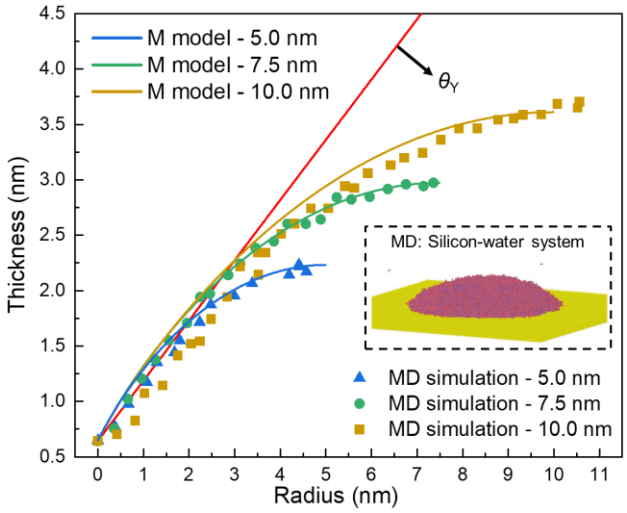

Fig. 2. Comparison of the droplet profiles on the nano-scale obtained from the M model and MD simulation simulations. θ_Y is the Young contact angle of a droplet on a silicon surface [60].

3. Results and discussions

3.1. Deviation of a 3D nano-droplet profile and interface nano-bending

We first start with the deviation of the nano-droplet profile. **Fig. 3a** shows the comparison between the microscopic droplet profile measured on hydroxylated glass in a recent experiment and a spherical shape profile [17]. The spherical shape profile is obtained by fitting the upper part of the droplet profile from the experiment. The microscopic droplet profile shows a deviation from the spherical shape near the contact line within the distance of several nanometers from the surface. This deviation was attributed only to the surface molecular forces [17,20]. **Fig. 3b** gives the sub-nano scale droplet profiles with different footprint radii by using MD simulation. The simulated droplet profiles also exhibit deviation from the spherical shape profile. In this case, the deviation is caused by the entangled effect of surface molecular forces and interface curvature. An interface nano-bending, which shows a concaving pattern on the sub-nanoscale (**Fig. 3b**) and a convex pattern on the nano-scale (**Fig. 2**), is formed near the contact line. This is similar to the experimental measurement as shown in **Fig. 3a**.

To investigate the relationship between the effect of surface molecular forces and the effect of the interface curvature, we compare the droplet profiles obtained by MD simulations and predictions by using Eq. 1 with the boundary condition of the Young contact angle on a silicon surface. From a mechanical perspective, the Young contact angle is defined at an inflection point

on the interface of a droplet with infinite size (2D) where the droplet profile transits from concave to convex in the transition region [59]. In the region with a concave profile, surface molecular forces dominate the droplet profile, while in the region with a convex profile, the hydrodynamic effect dominates. Therefore, the Young contact angle can be understood as a manifestation of surface molecular forces near the contact line. The prediction by Eq. 1 for the finite-size droplet (3D) can be interpreted as a linear superposition of the effect of the surface molecular forces and the effect of the local interface curvature on the interface. This method is pure hydrodynamics and has been widely adopted to calculate the droplet or liquid film profile [61,62]. In **Fig. 3b,** the red line represents the profile with infinite droplet size, and dashed lines give the predictions by Eq. 1 with the corresponding footprint radii of MD simulations. With the decrease of the footprint radii, the profiles deviate more from the red line because the capillary pressure induced by the larger curvature distorts the interface.

However, the droplet profiles by MD simulations deviate more from the red line with the increased footprint radii, which is in contrast to the calculated profiles by Eq. 1. This unexpected result implies the effect of surface molecular forces and the effect of the interface curvature on a 3D nano-droplet profile are nonlinearly coupled. In other words, any distortion of the droplet profile caused by one effect simultaneously influences the other one. Thus the interface nano-bending can be understood as a manifestation of the nonlinear-coupled effect near the contact line. The nonlinear-coupled effect may also be influenced by surface heterogeneities and external force fields that can further deform the interface. Therefore, the nonlinear-coupled effect is universal and demands consideration when modeling wetting phenomena.

3.2. Nonlinear-coupled effect

To understand the nonlinear-coupled effect, one must go through the manifestation of surface molecular forces in the interface nano-bending. For example, the 12-6 L-J intermolecular pair potential used in the MD simulation gives rise to surface molecular forces between the liquid-gas interface and the solid-liquid interface [52]. The gas-liquid interface experiences first repulsive force near the surface, and then attractive force when the interface is away from the surface. This qualitative description of the surface molecular forces explains the 3D droplet profile (**Fig. 3b**) obtained by MD simulation very well. However, to answer why the droplet profile deviates more from the red line with the increase of the footprint radii, we need to analyze the role of the interface

curvature. Considering an equilibrium droplet, the liquid pressure inside the droplet is uniform. According to Eq. 1, the droplet profile dominated by capillary pressure is convex and with smaller curvature when the footprint radii are larger. Therefore, the role of surface molecular forces and the interface curvature act in opposite ways within the range of repulsive surface molecular forces, while they both act to formulate a convex interface within the range of attractive surface molecular forces. As a result, the droplet profile on the sub-nanoscale deviates more with the increase of the footprint radii. A quantitative description of the nonlinear-coupled effect will rely on the analysis of the microlayer model in the next sections.

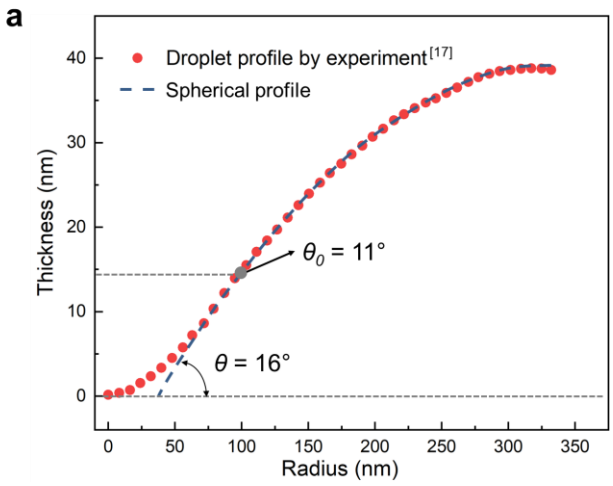

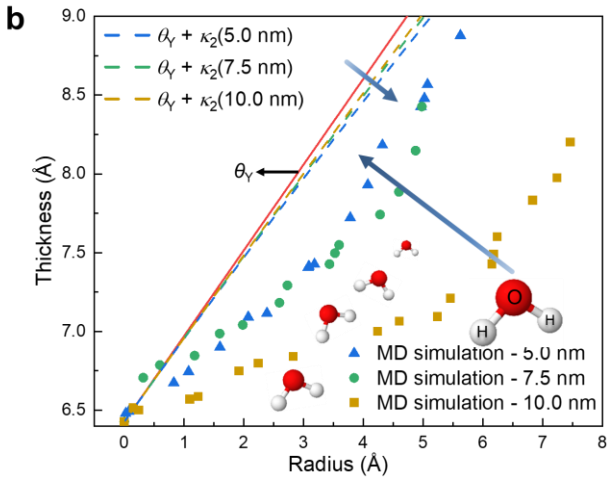

Fig. 3. Deviation of the 3D nano-droplet profile. (**a**) Comparison of the nano-droplet profile obtained from the experiment and a spherical shape. θ_0 is the contact angle at the inflection point obtained from the experiment [17]. θ is the contact angle obtained from the spherical shape profile.

(**b**) Comparison of the droplet profiles on the sub-nanoscale obtained from the MD simulations and Eq. 1. θ_Y is the Young contact angle of a droplet on a silicon surface, κ_2 is the principal curvature of the interface that is related to the droplet foorprint radii.

3.3. Profile of the microlayer in the inertia-controlled bubble growth stage

We model the microlayer profile in the inertia-controlled stage in nucleate boiling, also referred to as the initial stage [33]. The concept of the inertia-controlled stage was first proposed in a seminal paper by Mikic *et al.* [46]. In this stage, the bubble expands at a constant speed fueled by the overpressure of the vapor because its high internal pressure prevents the evaporation from the surrounding liquid under low superheat. In the last decade, the snapshots of the microlayer profile from several experiments using the laser interferometry method show that the formed microlayer profile remains almost stationary within a very short time (~0.6 ms) after the bubble nucleation [36,44]. This confirms ignorable evaporation from the microlayer at the beginning of the microlayer formation, namely, the inertia-controlled stage. Besides, the extrapolation of the microlayer profile indicates that there is no contact line movement, thus we can assume a no-slip boundary condition. The stationary microlayer allows us to avoid a transient microlayer in the inertia-controlled stage. As also shown in the literature [31], the interface of the microlayer evolves along with a fixed profile. In this work, we focus on the inertia-controlled stage, thus only the nonlinear-coupled effect and the hydrodynamic effect are considered in modeling the microlayer.

The nonlinear-coupled effect and the hydrodynamic effect are considered separately. We divide the microlayer into three regions (**Fig. 1b**): a molecular region, a transition region, and a hydrodynamic region. The nonlinear-coupled effect is accounted for in the molecular and transition region. The interface shape in these two regions can be described by Eq. 2. When a hemispherical bubble nucleus is trapped in a cavity with the radius r_c, the required superheat to activate the nucleate boiling is related to r_c [46]. In this work, we use r_c = 2.8 μm, for which the corresponding activation superheat is 12 K. In the transition region, surface molecular forces become less significant compared to the capillary pressure, thus we assume that the transition region ends when the capillary pressure is much larger (*e.g.*, 10 times) than surface molecular forces. The required two initial conditions at the contact line are given as $\delta_0 = 0.157\ nm$ [53] and

$\delta_0' = 0$, representing the adsorbed film thickness and the initial slope of the film profile. Parameters regarding the surface energy used in the M model are listed in **Table 2**.

Table 2. Surface energy components of studied surfaces.

Surface	γ^{LW} (mJ/m^2)	γ^+ (mJ/m^2)	γ^- (mJ/m^2)	Young CA (degree)	λ[54] (mm)
Glass[63]	38.2	1.2	49	23.80	0.4459
Silicon[60]	38.6	4	33.98	28.14	0.4613
ITO[64]	45.8	0	63.8	12.60	0.3434
Silica[65]	39.0	0.6	56	18.90	0.3871
Weakly hydrophilic	38.6	4	1.9	75.08	1.1256

Fig. 4a shows the microlayer profiles in the molecular and transition region on glass, silica, ITO, and silicon surfaces, all of which are calculated by the M model. These profiles vary in thickness due to the different surface energy. Nevertheless, we observe a fixed pattern of the profiles on each surface. The profile first exhibits a concaving pattern and then transits to convex with the slope starting to decrease continuously. This is because, within the nano-scale thickness of the microlayer, the repulsive and attractive molecular forces are dominant in turn. Together with the capillary pressure, a strong interface nano-bending presents within several nanometers of thickness, leading to a significant reduction of both profile thickness and slope in the molecular region. Such a nano-bending, analogy to that in the nano-droplet case, is a manifestation of the nonlinear-coupled effect between surface molecular forces and interface curvature. With the increase of the microlayer thickness, surface molecular forces decay rapidly and the capillary pressure becomes dominant, whereas the bending of the profiles becomes less significant, indicating the start of the hydrodynamic region.

For the hydrodynamic region of the microlayer, the hydrodynamic effect is dominant. Since the microlayer is very thin, we apply a lubrication approximation in cylindrical coordinates to describe the liquid flow in the microlayer. Here we derive an **H model** based on Nikolayev's approach [66], given as

$$\frac{\partial}{\partial r}\left[\delta\left(\frac{\delta}{2}+l_s\right)\frac{\partial \sigma}{\partial r}+\delta^2\left(\frac{\delta}{3}+l_s\right)\frac{\partial P_c}{\partial r}\right]=\mu\left(u^i-\frac{J}{\rho_L}\right). \quad (3)$$

l_s is the slip length of the liquid-solid interface, which is not considered in the microlayer in the inertia-controlled stage. u^i is the normal interface velocity and is considered to be positive if directed inside the liquid, $\frac{\partial \sigma}{\partial r}$ represents the Marangoni effect, and J is the mass evaporation flux at the interface. Considering the stationary microlayer profile [36] and nearly homogenous distributed temperature along the microlayer interface, u^i, $\frac{\partial \sigma}{\partial r}$, and J can be eliminated. Substitute the expression of the capillary pressure P_c into Eq. 3, the governing equation becomes

$$\frac{\partial}{\partial r}\left[\frac{\delta^3}{3}\frac{\partial}{\partial r}\left(\frac{\delta''}{(1+\delta'^2)^{\frac{3}{2}}}+\frac{\delta'}{r(1+\delta'^2)^{\frac{1}{2}}}\right)\sigma\right]=0. \quad (4)$$

Fig. 4a shows that the slope variation in the transition region is much weaker compared to that in the molecular region. Further, the experimental microlayer profiles [36,44,67] are approximately linear over the micron scale. This indicates the slope variation of the microlayer profile in the hydrodynamic region is very limited. Thus, we integrate Eq. 4 with respect to r and neglect the terms with second and third-order derivatives of δ. Then an analytical solution of Eq. 4 can be easily derived as

$$\delta=\sqrt[4]{C_1 r^3+C_2}, \quad (5)$$

with $C_1=-\frac{4C}{\sigma}$, $C_2=\delta_a^4+\frac{4C}{\sigma}r_a^3$, and $C=-\frac{\delta_a'\delta_a^3\sigma}{3r_a^2}$. C, C_1, and C_2 are the constants of integration. The subscript a represents an arbitrary position along the microlayer in the hydrodynamic region. Eq. 5 gives the microlayer profile in the hydrodynamic region. The derivation of the analytical solution Eq. 5 is included in the **Supporting Materials**.

According to Eq. 5, the microlayer thickness δ and the interface slope δ' at an arbitrary position along the microlayer are required to determine the constants C, C_1, and C_2. Here we develop a **hybrid model** that covers both the M model and H model by approximately matching the transition region and the hydrodynamic region. In other words, the molecular region and the transition region

are considered the inner boundary for the entire microlayer. We use the calculated results at the out end of the transition region by the M model to determine the constants of integration (see **Table S1** in the **Supporting Materials**). For surfaces of glass, silica, ITO, and silicon, C_1 has very close value, this indicates that the slopes of the microlayer profiles are similar on these surfaces. Furthermore, the calculated C_2 is much smaller than C_1, thus C_2 can be ignored given the millimeter-length microlayer. Now Eq. 5 reduces to $\delta = \sqrt[4]{C_1} r^{0.75}$. It has a similar form to Yabuki's expression $\delta = 5.10 \times 10^{-4} r^{0.69}$, which was obtained by fitting their experimental data [38]. **Fig. 4b** displays the microlayer profiles predicted by our hybrid model and the comparison with previous models and experiments [36–38]. The well-known models derived by Cooper and Smirnov follow from different hydrodynamic descriptions yet both relate the microlayer thickness to the bubble growth time [34,35], expressed as $\delta = C\sqrt{\nu t_g}$. The bubble growth time t_g can be related to the bubble growth speed. The constant C is obtained from an experimental fit and is proportional to the bubble growth speed. As shown in **Fig. 4b,** the results largely overestimate the microlayer thickness, that is, the hydrodynamic effect cannot "bend down" the microlayer effectively. The hybrid model successfully predicts the microlayer profile by considering a new inner boundary condition, which is derived based on the nonlinear-coupled effect.

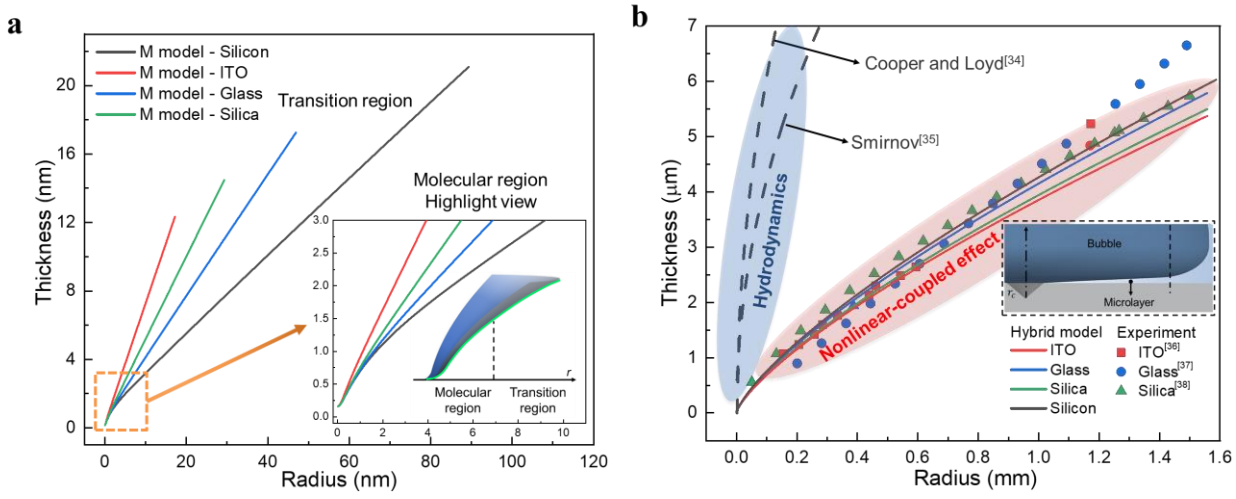

Fig. 4. Multiscale microlayer profile on various surfaces. (**a**) Microlayer profiles from the molecular region to the transition region on various surfaces predicted by the M model. (**b**) Full picture of the predicted microlayer profiles by the hybrid model and the comparison with previous

356 models and experiment data. Microlayer profile predictions in the blue region and red region are
357 based on the hydrodynamics and non-linear coupled effect, respectively.

358 *3.4. Deviation of the microlayer profile*

359 To understand how the nonlinear-coupled effect formulates the inner boundary condition for
360 the microlayer, we revisit the interface nano-bending in the molecular region (see **Fig. 4a** highlight
361 view). The repulsive surface molecular forces first raise the interface, and consequently, the effect
362 of the second principal curvature κ_2 is enhanced within the thickness of several angstroms. Note
363 that the capillary pressure induced by the second principal curvature increases the liquid pressure,
364 thus preventing the rise of the profile. With the increase in thickness, surface molecular forces turn
365 attractive. Together with the second principal curvature, both act to bend the profile downward.
366 The second principal curvature retards the decay of surface molecular forces and therefore
367 contributes to a further bending of the microlayer profile. The role of the nonlinear-coupled effect
368 differs from that in the nano-droplet. In the case of the microlayer, the coupling effectively
369 strengthens the role of both surface molecular forces and the interface curvature and becomes more
370 powerful in bending the profile.

371 We further consider a linear superposition of the impacts between surface molecular forces
372 and the interface curvature on the profile by bringing each into effect within two consecutive
373 regions starting from the contact line. In the first region, we only consider surface molecular forces
374 and the first principal curvature. We rewrite Eq. 2 as $P_v - P_l = \kappa_1 + P_d$ to describe the microlayer
375 profile. Similar to the interpretation of the Young contact angle of a 2D droplet [59], the Young
376 contact angle is formed in the first region. In the second region, the second principal curvature
377 takes effect and surface molecular forces vanish, the microlayer profile can be described as $P_v -$
378 $P_l = (\kappa_1 + \kappa_2)\sigma$. The boundary between these two regions is where the Young contact angle starts
379 to form in the first region, and the outer end of these two regions is considered to reach the same
380 slope as that at the outer end of the transition region in **Fig. 4a**. In this case, effects of the surface
381 molecular forces and the second principal curvature are linearly superposed, as we discussed in
382 the interpretation of Eq. 1. The calculated results are used to determine C_1 and C_2 in Eq. 5. We
383 show the microlayer profile with and without considering the nonlinear-coupled effect in **Fig. 5a**.
384 The microlayer thickness without the nonlinear-coupled effect reaches around 4.5 μm at 0.5 mm
385 microlayer length, almost 2 times higher than that with the nonlinear-coupled effect.

Next, we compare the predicted microlayer profiles with DNS simulations to elucidate the critical role of the inner boundary condition. As shown in **Fig. 5a**, the microlayer profile obtained by Guion *et al.* has a larger thickness [33]. On the other hand, the thickness of the microlayer profile in Ding's work is smaller [31] as there a smaller bubble nucleus size of 2 μm has been assumed compared to the 3 μm in Guion's work. It directly shows the significance of the bubble nucleus size. As indicated by the curvature expression $K = \frac{\delta''}{(1+\delta'^2)^{\frac{3}{2}}} + \frac{\delta'}{r(1+\delta'^2)^{\frac{1}{2}}}$, the capillary pressure induced by the second principal curvature would be extremely large with the smaller bubble nucleus. Such large capillary pressure can effectively "bend down" the microlayer. In the DNS simulation, the Young contact angle is imposed as the boundary condition, while in our hybrid model, δ'' is also included in the boundary condition and determines the entire microlayer profile implicitly through Eq. 4. The new boundary condition derived based on the nonlinear-coupled effect can be considered as a local pressure boundary condition, which is formulated by the sum of the interface curvature induced capillary pressure and the disjoining pressure in the molecular and transition region. From a perspective of the molecular force, the role of the nonlinear-coupled effect on the macroscale microlayer can be understood as that molecular forces by both water and surface are superimposed on the water-vapor interface in the molecular region and transmitted to the macroscale. In other words, the microlayer profile is a macroscale manifestation of the interaction between the solid surface and water molecules. Nevertheless, numerous previous works have also attempted to incorporate the augmented Young-Laplace equation in the DNS simulation of the microlayer.[41,68–71] Though as we discussed, the augmented Young-Laplace can account for the nonlinear-coupled effect, to the best of our knowledge, there is still no related report of the successful prediction of the microlayer profile. The most important reason is that a rather larger bubble nucleus was employed in these simulations, which overlooked the effect of the interface curvature.

Finally, we discuss the microlayer profile on a weakly hydrophilic surface. As shown in **Fig. 5b**, on a surface with the Young contact angle of 75.08° the microlayer thickness predicted by the hybrid model increases to ~10 μm at 0.5 mm length. Nevertheless, the required cavity radius (*i.e.*, nucleus size) to activate the nucleation is influenced by surface wettability. Previous studies based on thermodynamic analyses suggested a negative correlation between the critical cavity radius and surface wettability [72,73]. Thus, we assume a reduction of the cavity radius r_c on a weakly

hydrophilic surface. The results for r_c = 2.8, 1.0, 0.5 μm are plotted in **Fig. 5b**. When r_c decreases the thickness of the microlayer profile decreases too and the actual microlayer profile is met for $r_c = 0.5\ \mu m$. In addition, we can see a stronger impact of the nonlinear-coupled effect on weakly hydrophilic surfaces, because the radii of the second principal curvature are much smaller when the slope of the profile is larger.

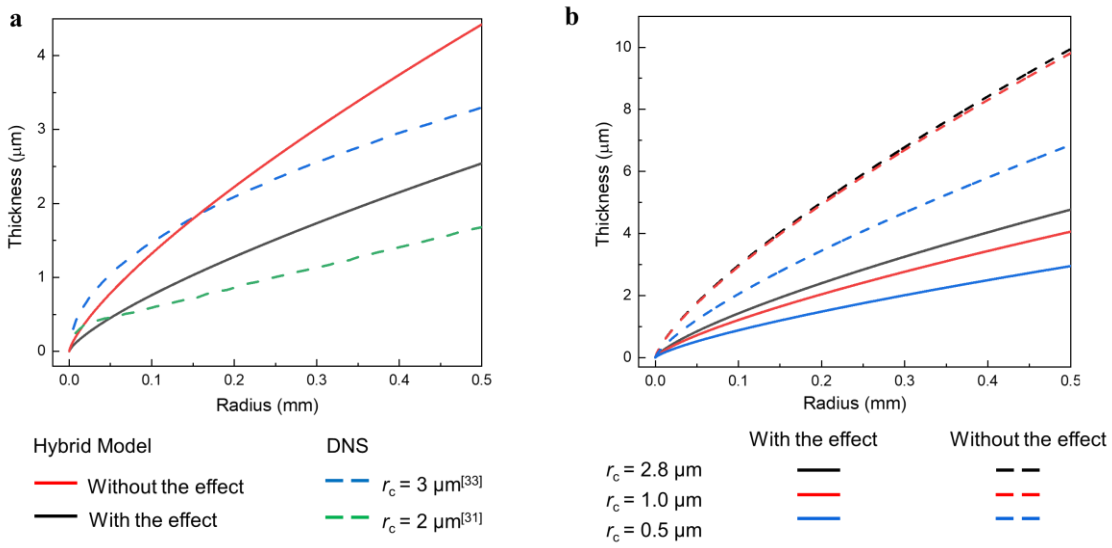

Fig. 5. Deviation of the microlayer profile. (**a**) Impact of the nonlinear-coupled effect on microlayer profile and comparison with DNS simulations. The green dashed line is from the simulation of Guion *et al.*; the blue dashed line is from the simulation of Ding *et al.* (**b**) Microlayer profile on the weakly hydrophilic surface with and without the nonlinear-coupled effect (Young contact angle = 75.08°).

4. Conclusions

In this work, we revealed a nonlinear-coupled effect between the liquid-gas interface geometry and the solid-liquid interactions in the microscopic liquid-wetting phenomenon. We performed MD simulations for nano-droplets to examine the nonlinear-coupled effect. Then we applied it in the multiscale modeling (M-Model, H-Model, and hybrid model) of a microlayer in the inertia-controlled bubble growth stage in nucleate boiling. The hybrid model successfully predicted the microlayer profile captured by different experiments [36–38] for the first time. We found that the nonlinear-coupled effect is responsible for the deviation of a nano-droplet profile from the prediction based on the conventional Young contact angle. Furthermore, the very thin microlayer

thickness in the inertia-controlled bubble growth stage is determined by the nonlinear-coupled effect, instead of the hydrodynamic effects considered in recent DNS simulation works [33,42,43].

The nonlinear-coupled effect explains the mechanism of the microscopic liquid-gas interface deviation from the prediction based on the conventional Young contact angle. We may therefore resolve the long-standing disputes over the validity of the Young contact angle at the nano-scale [28,74,75]. However, the detailed manifestations of the nonlinear-coupled effect depend on the liquid-gas geometries. In the context of the nano-droplet with the principal curvatures of the same signs (spherical shape), the impacts of the interface curvature and the solid-liquid interactions act in the opposite way within the repulsive range of surface molecular forces. In the context of the microlayer with the principal curvatures of the different signs (saddle shape), the nonlinear-coupled effect enhances the impacts of the interface curvature and solid-liquid interactions in bending the microlayer. It indicates that the nonlinear-coupled effect could play a more important role in bubble-related wetting phenomena, such as the long lifetime surface nano-bubble [76]. Moreover, the nonlinear-coupled effect structures an interface nano-bending near the surface that can be considered as a new pressure boundary condition for the liquid wetting system. The new pressure boundary condition enables us to unveil mechanisms behind recent intriguing microscopic wetting experiments. For example, the microscopic liquid film evaporation [8], and the surface curvature-driven microscopic droplet motion [6].

In future, it would be interesting to reinterpret the line tension based on the nonlinear-coupled effect so that the nonlinear dependency between the cosine of the contact angle of nano-droplets or surface nano-bubbles and the contact line curvature reported in many previous experimental studies [16,77] may be explained.

ACKNOWLEDGMENTS

The MD simulations were run on HEMERA, the HZDR's supercomputer. We acknowledge the support from the Guangzhou Elite Project.

CRediT authorship contribution statement

Jinming Zhang: Conceptualization, Methodology, Validation, Writing - original draft. **Wei Ding:** Conceptualization, Methodology, Writing - review & editing, Supervision. **Zuankai Wang:**

Writing – review & editing. **Hao Wang:** Methodology. **Uwe Hampel:** Conceptualization, Methodology, Writing - review & editing, Supervision. All authors have read and agreed to the published version of the manuscript.

Declaration of Competing Interest

The authors declare that they have no known competing financial interests or personal relationships that could have appeared to influence the work reported in this paper.

REFERENCES

[1] J. Hartmann, M.T. Schür, S. Hardt, Manipulation and control of droplets on surfaces in a homogeneous electric field, Nat. Commun. 13 (2022). https://doi.org/10.1038/s41467-021-27879-0.

[2] D. Soltman, B. Smith, S.J.S. Morris, V. Subramanian, Inkjet printing of precisely defined features using contact-angle hysteresis, J. Colloid Interface Sci. 400 (2013) 135–139. https://doi.org/10.1016/j.jcis.2013.03.006.

[3] H. Cha, H. Vahabi, A. Wu, S. Chavan, M.K. Kim, S. Sett, S.A. Bosch, W. Wang, A.K. Kota, N. Miljkovic, Dropwise condensation on solid hydrophilic surfaces, Sci. Adv. 6 (2020). https://doi.org/10.1126/sciadv.aax0746.

[4] X. Dai, N. Sun, S.O. Nielsen, B.B. Stogin, J. Wang, S. Yang, T.S. Wong, Hydrophilic directional slippery rough surfaces for water harvesting, Sci. Adv. 4 (2018) 1–11. https://doi.org/10.1126/sciadv.aaq0919.

[5] S. Feng, P. Zhu, H. Zheng, H. Zhan, C. Chen, J. Li, L. Wang, X. Yao, Y. Liu, Z. Wang, Three-dimensional capillary ratchet-induced liquid directional steering, Science. 373 (2021) 1344–1348. https://doi.org/10.1126/science.abg7552.

[6] C. Lv, C. Chen, Y.C. Chuang, F.G. Tseng, Y. Yin, F. Grey, Q. Zheng, Substrate curvature gradient drives rapid droplet motion, Phys. Rev. Lett. 113 (2014) 1–5. https://doi.org/10.1103/PhysRevLett.113.026101.

[7] B. Radha, A. Esfandiar, F.C. Wang, A.P. Rooney, K. Gopinadhan, A. Keerthi, A. Mishchenko, A. Janardanan, P. Blake, L. Fumagalli, M. Lozada-Hidalgo, S. Garaj, S.J. Haigh, I. V. Grigorieva, H.A. Wu, A.K. Geim, Molecular transport through capillaries made with atomic-scale precision, Nature. 538 (2016) 222–225. https://doi.org/10.1038/nature19363.

[8] Y. Li, M.A. Alibakhshi, Y. Zhao, C. Duan, Exploring Ultimate Water Capillary Evaporation in Nanoscale Conduits, Nano Lett. 17 (2017) 4813–4819. https://doi.org/10.1021/acs.nanolett.7b01620.

[9] D. Jiang, Z. Fan, H. Wang, M. Xu, G. Chen, Y. Song, Z.L. Wang, Triboelectric nanogenerator powered electrowetting-on-dielectric actuator for concealed aquatic microbots, ACS Nano. 14 (2020) 15394–15402. https://doi.org/10.1021/acsnano.0c05901.

[10] Y. Wang, S. Gao, W. Xu, Z. Wang, Nanogenerators with Superwetting Surfaces for Harvesting Water/Liquid Energy, Adv. Funct. Mater. 30 (2020). https://doi.org/10.1002/adfm.201908252.

[11] D. Bonn, J. Eggers, J. Indekeu, J. Meunier, Wetting and spreading, Rev. Mod. Phys. 81 (2009) 739–805. https://doi.org/10.1103/RevModPhys.81.739.

[12] A. Marmur, Solid-surface characterization by wetting, Annu. Rev. Mater. Res. 39 (2009) 473–489. https://doi.org/10.1146/annurev.matsci.38.060407.132425.

[13] H. Wang, From Contact Line Structures to Wetting Dynamics, Langmuir. 35 (2019) 10233–10245. https://doi.org/10.1021/acs.langmuir.9b00294.

[14] A. Moldovan, P.M. Bota, T. Dan Poteca, I. Boerasu, D. Bojin, D. Buzatu, M. Enachescu, Scanning polarization force microscopy investigation of contact angle and disjoining pressure of glycerol and sulfuric acid on highly oriented pyrolytic graphite and aluminum, EPJ Appl. Phys. 64 (2013) 1–7. https://doi.org/10.1051/epjap/2013130235.

[15] T. Pompe, S. Herminghaus, Three-phase contact line energetics from nanoscale liquid surface topographies, Phys. Rev. Lett. 85 (2000) 1930–1933. https://doi.org/10.1103/PhysRevLett.85.1930.

[16] A. Checco, P. Guenoun, J. Daillant, Nonlinear dependence of the contact angle of nanodroplets on contact line curvature, Phys. Rev. Lett. 91 (2003) 1–4. https://doi.org/10.1103/PhysRevLett.91.186101.

[17] F. Samoila, L. Sirghi, Disjoining Pressure in Partial Wetting on the Nanoscale, Langmuir. 33 (2017) 5188–5196. https://doi.org/10.1021/acs.langmuir.7b01156.

[18] P.C. Wayner Jr, The effect of interfacial mass transport on flow in thin liquid films, Colloids and Surfaces. 52 (1991) 71–84. http://www.scopus.com/inward/record.url?eid=2-s2.0-0026060309&partnerID=40&md5=050cabcb8304a02f45dc463caca00df7.

[19] S. Narayanan, A.G. Fedorov, Y.K. Joshi, Interfacial transport of evaporating water confined in nanopores, Langmuir. 27 (2011) 10666–10676. https://doi.org/10.1021/la201807a.

[20] P.G.D. Gennes, X. Hua, P. Levinson, Dynamics of wetting: Local contact angles, J. Fluid

Mech. 212 (1990) 55–63. https://doi.org/10.1017/S0022112090001859.

[21] H. Wang, L. Chen, A general model for dynamic contact angle over full speed regime, ArXiv. (2019) 4–6.

[22] Z. Lu, S. Narayanan, E.N. Wang, Modeling of Evaporation from Nanopores with Nonequilibrium and Nonlocal Effects, Langmuir. 31 (2015) 9817–9824. https://doi.org/10.1021/acs.langmuir.5b01700.

[23] R.J. Good, M.N. Koo, The effect of drop size on contact angle, J. Colloid Interface Sci. 71 (1979) 283–292. https://doi.org/10.1016/0021-9797(79)90239-X.

[24] J. Park, H.S. Han, Y.C. Kim, J.P. Ahn, M.R. Ok, K.E. Lee, J.W. Lee, P.R. Cha, H.K. Seok, H. Jeon, Direct and accurate measurement of size dependent wetting behaviors for sessile water droplets, Sci. Rep. 5 (2015) 1–13. https://doi.org/10.1038/srep18150.

[25] A. Setchi, Y. Chen, J. Yu, H. Wang, Structural effects in partially-wetting thin evaporating liquid films near the contact line, Int. J. Heat Mass Transf. 132 (2019) 420–430. https://doi.org/10.1016/j.ijheatmasstransfer.2018.11.151.

[26] L. Schimmele, M. Naplórkowski, S. Dietrich, Conceptual aspects of line tensions, J. Chem. Phys. 127 (2007). https://doi.org/10.1063/1.2799990.

[27] M. Kanduč, L. Eixeres, S. Liese, R.R. Netz, Generalized line tension of water nanodroplets, Phys. Rev. E. 98 (2018) 1–6. https://doi.org/10.1103/PhysRevE.98.032804.

[28] J. Zhang, P. Wang, M.K. Borg, J.M. Reese, D. Wen, A critical assessment of the line tension determined by the modified Young's equation, Phys. Fluids. 30 (2018).

https://doi.org/10.1063/1.5040574.

[29] A. Amirfazli, A.W. Neumann, Status of the three-phase line tension: A review, Adv. Colloid Interface Sci. 110 (2004) 121–141. https://doi.org/10.1016/j.cis.2004.05.001.

[30] J. Kim, Review of nucleate pool boiling bubble heat transfer mechanisms, Int. J. Multiph. Flow. 35 (2009) 1067–1076. https://doi.org/10.1016/j.ijmultiphaseflow.2009.07.008.

[31] W. Ding, J. Zhang, D. Sarker, U. Hampel, The role of microlayer for bubble sliding in nucleate boiling: A new viewpoint for heat transfer enhancement via surface engineering, Int. J. Heat Mass Transf. 149 (2020) 119239. https://doi.org/10.1016/j.ijheatmasstransfer.2019.119239.

[32] D.I. Yu, H.J. Kwak, H. Noh, H.S. Park, K. Fezzaa, M.H. Kim, Synchrotron x-ray imaging visualization study of capillary-induced flow and critical heat flux on surfaces with engineered micropillars, Sci. Adv. 4 (2018) 3–6. https://doi.org/10.1126/sciadv.1701571.

[33] A. Guion, S. Afkhami, S. Zaleski, J. Buongiorno, Simulations of microlayer formation in nucleate boiling, Int. J. Heat Mass Transf. 127 (2018) 1271–1284. https://doi.org/10.1016/j.ijheatmasstransfer.2018.06.041.

[34] M.G. Cooper, A.J.P. Lloyd, The microlayer in nucleate pool boiling, Int. J. Heat Mass Transf. 12 (1969) 895–913. https://doi.org/10.1016/0017-9310(69)90154-9.

[35] G.F. Smirnov, Calculation of the “initial” thickness of the “microlayer” during bubble boiling, J. Eng. Phys. 28 (1975) 369–374. https://doi.org/10.1007/BF00862021.

[36] S. Jung, H. Kim, Hydrodynamic formation of a microlayer underneath a boiling bubble, Int.

J. Heat Mass Transf. 120 (2018) 1229–1240. https://doi.org/10.1016/j.ijheatmasstransfer.2017.12.098.

[37] Y. Utaka, Y. Kashiwabara, M. Ozaki, Microlayer structure in nucleate boiling of water and ethanol at atmospheric pressure, Int. J. Heat Mass Transf. 57 (2013) 222–230. https://doi.org/10.1016/j.ijheatmasstransfer.2012.10.031.

[38] T. Yabuki, O. Nakabeppu, Heat transfer mechanisms in isolated bubble boiling of water observed with MEMS sensor, Int. J. Heat Mass Transf. 76 (2014) 286–297. https://doi.org/10.1016/j.ijheatmasstransfer.2014.04.012.

[39] S. Hänsch, S. Walker, Microlayer formation and depletion beneath growing steam bubbles, Int. J. Multiph. Flow. 111 (2019) 241–263. https://doi.org/10.1016/j.ijmultiphaseflow.2018.11.004.

[40] G. Giustini, S. Jung, H. Kim, K.H. Ardron, S.P. Walker, Microlayer evaporation during steam bubble growth, Int. J. Therm. Sci. 137 (2019) 45–54. https://doi.org/10.1016/j.ijthermalsci.2018.11.012.

[41] J. Bhati, S. Paruya, Numerical simulation of bubble dynamics in pool boiling at heated surface, Int. J. Heat Mass Transf. 152 (2020) 119465. https://doi.org/10.1016/j.ijheatmasstransfer.2020.119465.

[42] A. Urbano, S. Tanguy, G. Huber, C. Colin, Direct numerical simulation of nucleate boiling in micro-layer regime, Int. J. Heat Mass Transf. 123 (2018) 1128–1137. https://doi.org/10.1016/j.ijheatmasstransfer.2018.02.104.

[43] L. Bureš, Y. Sato, On the modelling of the transition between contact-line and microlayer evaporation regimes in nucleate boiling, J. Fluid Mech. 916 (2021) 1–23. https://doi.org/10.1017/jfm.2021.204.

[44] Z. Chen, A. Haginiwa, Y. Utaka, Detailed structure of microlayer in nucleate pool boiling for water measured by laser interferometric method, Int. J. Heat Mass Transf. 108 (2017) 1285–1291. https://doi.org/10.1016/j.ijheatmasstransfer.2017.01.003.

[45] M. Gao, L. Zhang, P. Cheng, X. Quan, An investigation of microlayer beneath nucleation bubble by laser interferometric method, Int. J. Heat Mass Transf. 57 (2013) 183–189. https://doi.org/10.1016/j.ijheatmasstransfer.2012.10.017.

[46] B.B. Mikic, W.M. Rohsenow, P. Griffith, On bubble growth rates, Int. J. Heat Mass Transf. 13 (1970) 657–666. https://doi.org/10.1016/0017-9310(70)90040-2.

[47] S. Plimpton, Fast Parallel Algorithms for Short-Range Molecular Dynamics, J. Comput. Phys. 117 (1995) 1–19. https://doi.org/10.1006/jcph.1995.1039.

[48] B. Ramos-Alvarado, S. Kumar, G.P. Peterson, Wettability of graphitic-carbon and silicon surfaces: MD modeling and theoretical analysis, J. Chem. Phys. 143 (2015). https://doi.org/10.1063/1.4927083.

[49] B. V. Derjaguin, N. V. Churaev, On the question of determining the concept of disjoining pressure and its role in the equilibrium and flow of thin films, J. Colloid Interface Sci. 66 (1978) 389–398. https://doi.org/10.1016/0021-9797(78)90056-5.

[50] I. V. Kuchin, O.K. Matar, R. V. Craster, V.M. Starov, Influence of the Disjoining Pressure

607 on the Equilibrium Interfacial Profile in Transition Zone Between a Thin Film and a
608 Capillary Meniscus, Colloids Interface Sci. Commun. 1 (2014) 18–22.
609 https://doi.org/10.1016/j.colcom.2014.06.002.

610 [51] J.A. Schonberg, S. DasGupta, P.C. Wayner, An augmented Young-Laplace model of an
611 evaporating meniscus in a microchannel with high heat flux, Exp. Therm. Fluid Sci. 10
612 (1995) 163–170. https://doi.org/10.1016/0894-1777(94)00085-M.

613 [52] J.N. Israelachvili, Intermolecular and Surface Forces, 3rd ed., Elsevier, 2011.
614 https://linkinghub.elsevier.com/retrieve/pii/C20090215601.

615 [53] C.J. van Oss, The Properties of Water and their Role in Colloidal and Biological Systems,
616 1st ed., Academic Press, 2008.

617 [54] N. V. Churaev, V.D. Sobolev, Wetting of low-energy surfaces, Adv. Colloid Interface Sci.
618 134–135 (2007) 15–23. https://doi.org/10.1016/j.cis.2007.04.012.

619 [55] M.U. Hammer, T.H. Anderson, A. Chaimovich, M.S. Shell, J. Israelachvili, The search for
620 the hydrophobic force law, Faraday Discuss. 146 (2012) 299–308.
621 https://www.ncbi.nlm.nih.gov/pmc/articles/PMC3624763/pdf/nihms412728.pdf.

622 [56] O. Arjmandi-Tash, N.M. Kovalchuk, A. Trybala, I. V. Kuchin, V. Starov, Kinetics of
623 Wetting and Spreading of Droplets over Various Substrates, Langmuir. 33 (2017) 4367–
624 4385. https://doi.org/10.1021/acs.langmuir.6b04094.

625 [57] A. Majumdar, I. Mezic, Instability of ultra-thin water films and the mechanism of droplet
626 formation on hydrophilic surfaces, J. Heat Transfer. 121 (1999) 964–971.

https://doi.org/10.1115/1.2826087.

[58] C.J. Van Oss, Long-range and short-range mechanisms of hydrophobic attraction and hydrophilic repulsion in specific and aspecific interactions, J. Mol. Recognit. 16 (2003) 177–190. https://doi.org/10.1002/jmr.618.

[59] M. Elena Diaz, J. Fuentes, R.L. Cerro, M.D. Savage, An analytical solution for a partially wetting puddle and the location of the static contact angle, J. Colloid Interface Sci. 348 (2010) 232–239. https://doi.org/10.1016/j.jcis.2010.04.030.

[60] D.J. Preston, Y. Song, Z. Lu, D.S. Antao, E.N. Wang, Design of Lubricant Infused Surfaces, ACS Appl. Mater. Interfaces. 9 (2017) 42383–42392. https://doi.org/10.1021/acsami.7b14311.

[61] P.D. Ravazzoli, I. Cuellar, A.G. González, J.A. Diez, Contact-angle-hysteresis effects on a drop sitting on an incline plane, Phys. Rev. E. 99 (2019) 043105. https://doi.org/10.1103/PhysRevE.99.043105.

[62] V. Janeček, V.S. Nikolayev, Contact line singularity at partial wetting during evaporation driven by substrate heating, Epl. 100 (2012). https://doi.org/10.1209/0295-5075/100/14003.

[63] A. Kowalski, Z. Czech, Ł. Byczyński, How does the surface free energy influence the tack of acrylic pressure-sensitive adhesives (PSAs)?, J. Coatings Technol. Res. 10 (2013) 879–885. https://doi.org/10.1007/s11998-013-9522-2.

[64] E.M. Harnett, J. Alderman, T. Wood, The surface energy of various biomaterials coated with adhesion molecules used in cell culture, Colloids Surfaces B Biointerfaces. 55 (2007)

90–97. https://doi.org/10.1016/j.colsurfb.2006.11.021.

[65] D. Aronov, G. Rosenman, Surface energy modification by electron beam, Surf. Sci. 601 (2007) 5042–5049. https://doi.org/10.1016/j.susc.2007.09.003.

[66] V.S. Nikolayev, Dynamics of the triple contact line on a nonisothermal heater at partial wetting, Phys. Fluids. 22 (2010). https://doi.org/10.1063/1.3483558.

[67] S. Jung, H. Kim, An experimental method to simultaneously measure the dynamics and heat transfer associated with a single bubble during nucleate boiling on a horizontal surface, Int. J. Heat Mass Transf. 73 (2014) 365–375. https://doi.org/10.1016/j.ijheatmasstransfer.2014.02.014.

[68] G. Son, V.K. Dhir, N. Ramanujapu, Dynamics and heat transfer associated with a single bubble during nucleate boiling on a horizontal surface, J. Heat Transfer. 121 (1999) 623–631. https://doi.org/10.1115/1.2826025.

[69] D.M. Christopher, L. Zhang, Heat transfer in the microlayer under a bubble during nucleate boiling, Tsinghua Sci. Technol. 15 (2010) 404–413. https://doi.org/10.1016/S1007-0214(10)70080-8.

[70] E. Aktinol, V.K. Dhir, T. Jaeger, W. Mirczak, Numerical simulations of nucleate boiling and film condensation heat transfer in a fixed-volume chamber in microgravity, Int. J. Heat Mass Transf. 132 (2019) 886–905. https://doi.org/10.1016/j.ijheatmasstransfer.2018.11.125.

[71] V.K. Dhir, G.R. Warrier, E. Aktinol, Numerical simulation of pool boiling: A review, J.

667 Heat Transfer. 135 (2013). https://doi.org/10.1115/1.4023576.

668 [72] X. Quan, G. Chen, P. Cheng, A thermodynamic analysis for heterogeneous boiling
669 nucleation on a superheated wall, Int. J. Heat Mass Transf. 54 (2011) 4762–4769.
670 https://doi.org/10.1016/j.ijheatmasstransfer.2011.05.026.

671 [73] S.G. Bankoff, Entrapment of gas in the spreading of a liquid over a rough surface, AIChE
672 J. 4 (1958) 24–26. https://doi.org/10.1002/aic.690040105.

673 [74] D. Seveno, T.D. Blake, J. De Coninck, Young's equation at the nanoscale, Phys. Rev. Lett.
674 111 (2013). https://doi.org/10.1103/PhysRevLett.111.096101.

675 [75] T. Ingebrigtsen, S. Toxvaerd, Contact angles of Lennard-Jones liquids and droplets on
676 planar surfaces, J. Phys. Chem. C. 111 (2007) 8518–8523.
677 https://doi.org/10.1021/jp0676235.

678 [76] D. Lohse, X. Zhang, Surface nanobubbles and nanodroplets, Rev. Mod. Phys. 87 (2015)
679 981–1035. https://doi.org/10.1103/RevModPhys.87.981.

680 [77] N. Kameda, S. Nakabayashi, Size-induced sign inversion of line tension in nanobubbles at
681 a solid/liquid interface, Chem. Phys. Lett. 461 (2008) 122–126.
682 https://doi.org/10.1016/j.cplett.2008.07.012.

683

684